UAV hyperspectral image acquisition and processing, an application for nutrient estimation of rice in Vietnam

Minh Khanh Luong[1], Tong Si Son[1*], Huong Mai[1], Huong Thi Mai To[1], Giang Son Tran[1], Binh Pham-Duc[1], Hien Phan[1], Le Van Canh[2], Thi Lan Pham[2], Tong Thi Huyen Ai[3]

[1]*University of Science and Technology of Hanoi (USTH), VAST, Hanoi, Vietnam*
[2]*Hanoi University of Mining and Geology (HUMG), Hanoi, Vietnam*
[3]*Space Technology Institute (STI), VAST, Hanoi, Vietnam*

ABSTRACT

Hyperspectral imagery obtained from Unmanned Aerial Vehicles (UAVs) is increasingly employed to investigate nutrient concentrations in vegetation. The deployment of a hyperspectral camera on a UAV, flight planning, image acquisition, preprocessing of hyperspectral data, and the subsequent estimation of nutrient concentrations in vegetation are facing challenges. These challenges manifest as geometric, spectral distortions and the abundance of numerous spectral bands. This study seeks to guide the mitigation of the impact of issues encountered during an experiment to estimate nutrient concentrations in rice leaves using UAV hyperspectral images. An industrial hexagonal drone equipped with a push-broom hyperspectral camera featuring 122 bands within the Visible to Near-Infrared (VIS-NIR) wavelength range (400-960 nm) is employed to collect data over a 1-hectare testing rice field. Models for estimating Leaf Phosphorus Concentration (LPC) and Leaf Potassium Concentration (LKC) are developed based on the correlation between hyperspectral images, characterized by a 3 cm spatial resolution, and 162 LPC and 162 LKC reference data points. The outcomes of utilizing various vegetation indices for LPC and LKC estimation reveal that a combination of band wavelengths at 838 nm and 734 nm is effective for LPC estimation, yielding a Root Mean Square Error (RMSE) of 27.1%. Conversely, LKC estimation exhibits an RMSE of 38.8% with an insignificant correlation between LKC and the current wavelength ranges. Above all, this study is a primary example of using UAV hyperspectral data in precision agriculture in Vietnam.

Keywords: Unmanned Aerial Vehicle, Hyperspectral remote sensing, Nutrient concentration, Vegetation indices.

1. Introduction

Rice provides a vital part of nutrition for over half of the population in the world (Wallach, 2022). Monitoring the health of the rice is an essential demand to maintain and increase the production of rice products. The amount of nutrients, especially nitrogen (N), phosphorous (P), and potassium (K) accumulated inside rice leaves is linked directly to the plant's yield. Low N, P, and K concentration levels can cause losses in the quality and quantity of rice yield. In contrast, excess N, P, and K can cause overgrowth, reducing the strength of stems and attracting insects, pathogens, and fungi (Campos-Soriano et al., 2020; Buresh, 2022). Nitrogen fertilizer can increase plant height, panicle number, spbikelet number, and the number of filled spikelet, all of which influence rice

*Corresponding author, Email: tong-si.son@usth.edu.vn

yield capacity (Dobermann and Fairhurst, 2000). Phosphorus is essential for root growth, early flowering and ripening, and resistance to disease and drought conditions. Phosphorus deficiency may cause rice plant maturity to be delayed and increase susceptibility to rice disease (Hindersah et al., 2022). Potassium application is closely related to the lignification of sclerenchyma cells, vascular bundles, and culm strength, all of which improve lodging resistance (Hindersah et al., 2022). The deficiency or sufficiency of N, P, and K alters the chemical components of rice leaves, affecting the spectral reflectance signature of leaves or canopy (Sanchez et al., 2020). Conversely, the color, shape, and sheath of leaves indicate the nutrient and health status of the plant, which is closely related to the nutrition content.

Although it can give an exact result, analyzing nutrient concentration using the chemical approach is a high-cost, time-consuming process and is limited to specific rice plots. During growth stages, the nutrient balance process must happen precisely in time, and applying chemical analysis is a problematic solution for a large rice field. Remote sensing is a practical approach for monitoring rice health due to its rapid, non-intrusive nature and capability to cover extensive areas of crops (Delavarpour et al., 2021). Diagnostic methods based on rice's spectral signature that use hyper-spectral imaging techniques can dynamically and quantitatively extract nutrition status (Stuart 2021). Hyperspectral imaging collects and processes reflectance signatures to generate hundreds of spectral bands to find objects, identify materials (Chang, 2003; Grahn and Geladi, 2007), or analyze plant chemical properties (Ling et al., 2019). A hyperspectral imager integrated into a crewless aerial vehicle (UAV) acquires hyperspectral images with a centimeter-level of spatial resolution below cloud layers; repeatable acquisition at any stage of vegetation growth is a potential approach for precision agriculture (Delavarpour et al., 2021).

UAV hyperspectral images have been used for determining leave nitro concentration (LNC) (Wang et al., 2021) and leave potassium concentration (LKC) with a small plot experiment (5 × 6 m) (Lu et al., 2020) but no leave phosphorus concentration (LPC) in rice. However, the applications of UAV-hyperspectral imagers face difficulties in appropriately assembling the UAV system's components for image acquisition, preprocessing images, and constructing models for estimating nutrient concentration from hyperspectral data (Adão et al., 2017).

In Vietnam, various applications of satellite images for investigating different aspects of rice, such as rice productivity (Clauss et al., 2018), rice mapping (Nguyen et al., 2015), and rice growth status (Phung et al., 2020). Hyperspectral data, particularly from UAV-based hyperspectral systems, is a gap in measuring nutrient concentration in rice leaves due to limitations in data acquisition equipment and processing techniques.

The present study aims to provide instruction on deploying a UAV hyperspectral imaging system to investigate the nutrient concentration in rice leaves. The experiment is implemented in sample rice fields designed to plant rice with different amounts of N, P, and K in fertilizer. Problems, difficulties, and solutions in integrating the UAV hyperspectral image system components, UAV hyperspectral image acquisition, and preprocessing images are characterized in detail. Subsequently, the relationship of LPC and LKC with their respective hyperspectral reflectance is analyzed to identify LPC, LKC responsive wavelengths for estimating these nutrients from hyperspectral images.

2. Study area and Material

2.1. Experimental site

A test field was established in Lam Thao district, Phu Tho province, Vietnam, at coordinates 21.2765°N, 105.3335°E. Located in the northern part of Vietnam within the Red

River delta, the area is characterized by tropical weather and receives an annual rainfall of 1,720 mm. Residents have traditionally cultivated rice in this region. The sample rice field is arranged into 54 square parcels, each 100 m^2. Rice parcels are fertilized with a different amounts of N, P, and K to cause the variation of leaf nutrient concentration. Two species of rice, J02 and TBR225, popularly seeded in Vietnam, are equally planted in the fields, with 27 parcels for planting J02 and 27 for TBR225 (Fig. 1). For each parcel, three points are evenly selected along one of the two diagonals to measure spectral reflectance and to collect leaf samples for analyzing nutrient concentrations. The rice field is cared for during the growing stages to ensure no significant crop harm due to water stress or diseases. At the time of image acquisition, rice is in the panicle initiation stage with a height ranging between 0.6 m and 0.9 m. This stage marks the end of the tillering or vegetative phase and the beginning of the reproductive phase with a full crop canopy.

Figure 1. The sample field with 54 rice parcels named "T" and "J" letters corresponding to TBR225 and J02 rice species, respectively

2.2. UAV hyperspectral system

The UAV hyperspectral system used in the study is integrated of 3 independent subsystems: a UAV to grab the whole system, a gimble system to control the camera orientation, and a hyperspectral data acquisition system including a camera to acquire images, a next unit of computing (NUC) to monitor the camera, and a global navigation satellite system (GNSS) receiver to record real-time positions of the camera (Fig. 2). All subsystems must be appropriately assimilated before image acquisition.
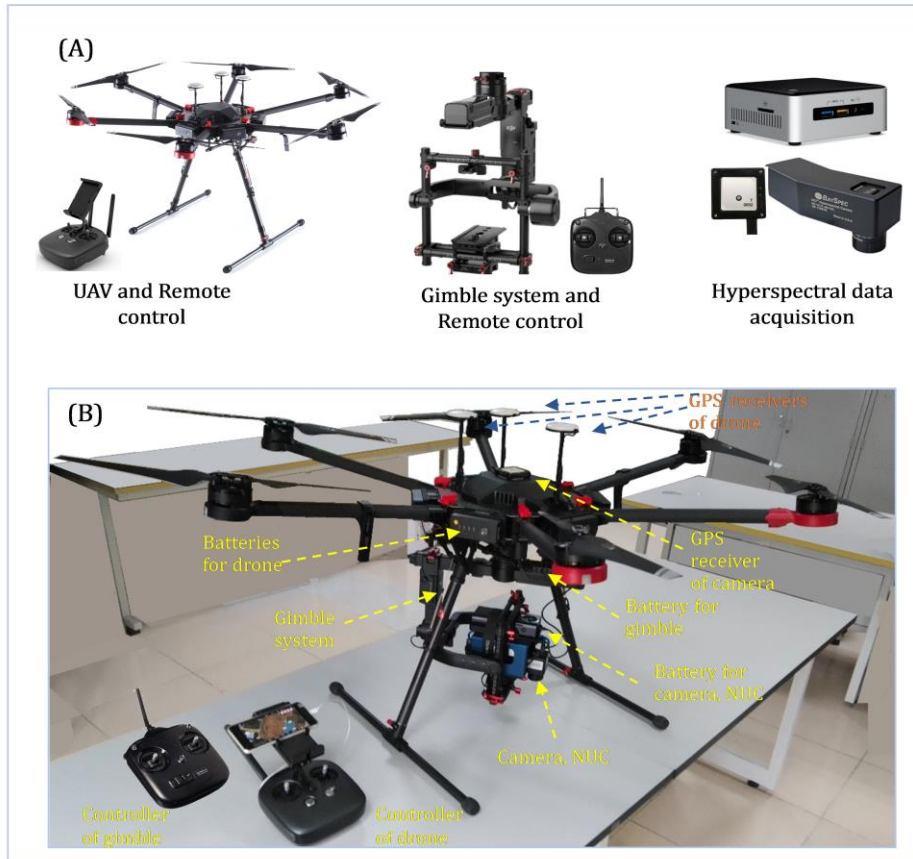
Figure 2. (A) Three subsystems of a UAV hyperspectral system the platform, the gimble system, and the hyperspectral data acquisition. (B) All subsystems are fully assembled in a UAV hyperspectral system

2.2.1. UAV platform and Gimble system

To ensure the ability to grab the whole hyperspectral system acquiring images, an industrial hexagonal drone, DJI Matrice 600 Pro, with a takeoff weight of 15.5 kg, is used for the experiment. The drone is relatively large and requires strictly safe conditions for flight missions. The DJI GO app can visualize flight paths and control the drone to make maps.

A gimble stabilization system keeps the payload in the planned orientation during the fights. The DJI Ronin-MX gimble used in the study is typically compatible with the drone and operates independently of the drone. The gimble system includes various sensors, brushless motors moving on three axes, batteries, and remote control to control the pan, roll, and tilt movement of the payload automatically or manually. For a UAV remote sensing system, the payload and the drone can be flexibly integrated by the gimble with a set of horizontal and vertical adjustment locks.

2.2.2. Hyperspectral Imager System

A hyperspectral camera OCI-F is used to achieve the hyperspectral images for the study. The camera is compact and lightweight (570 g) to operate on the ground or with a UAV platform. The charge-coupled device (CCD) sensor of the OCI-F camera comprises 800 lined detectors operating in full push-broom mode, covering the visible and near-

infrared wavelength range from 400 nm to 960 nm. The camera generates 122 image bands with a bandwidth of 5 nm for every data frame and 60 frames in a second.

NUC computer, a minicomputer installed with the SpecGrabber software, is integrated into the imager system for calibrating, setting up parameters, and operating the hyperspectral camera. The camera and a global navigation satellite system (GNSS) receiver are connected to the NUC to form a payload. Besides, a rechargeable battery supplies energy for the regular accomplishment of the subsystem.

A compacted GNSS receiver for real-time geotagging on hyperspectral data is mounted on the drone's top and connected to the NUC via a USB cable. This GNSS receiver is different from the drone's GNSS receivers. Every data frame's coordinates (latitude, longitude, and altitude) are recorded to process hyperspectral images.

3. Methodology

This study is based on three primary methodologies: UAV hyperspectral data acquisition, hyperspectral image preprocessing, and estimation of nutrient concentrations in rice leaves from hyperspectral images (Fig. 3).
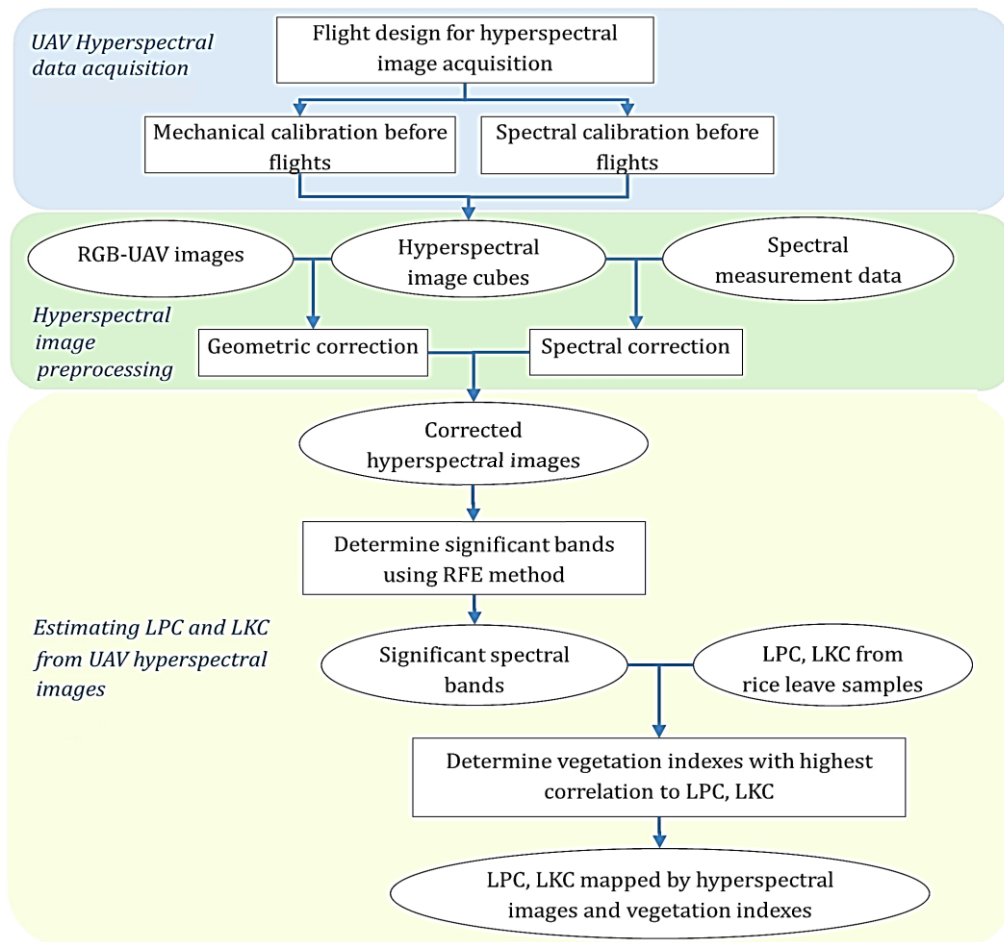

Figure 3. Schematic representation of the study methods, with ellipses denoting results or data and rectangles representing processes

3.1. Calculate flight parameters

To design flight paths for a hyperspectral acquisition, some equations are introduced to help users calculate basic flight parameters such as the flying height (H'), the distance between flight lines' centers (C), and the number of flight lines (NL).

$$H' = f \times \frac{GSD}{p} \qquad (1)$$

$$C = GSD \times N \times \left(\frac{100 - S}{100}\right) \qquad (2)$$

$$NL = \frac{W}{C} + 2 \qquad (3)$$

where f is the focal length; p is the detector size;

GSD is ground sampling distance (GSD), the so-called spatial resolution; N is the number of lined detectors in the sensor; S is the percent of side overlap between two swath sizes defined by adjacent flight lines; W is the width of the study area.

The hyperspectral camera has a focal length of 16 cm, a field of view of 24°, and a detector size of 5.3×10^{-6} m. To take hyperspectral images with a 0.03 m spatial resolution, covering the study area of 134 × 120 m size, the drone is designed to fly at a 90 m flight height with 11 light lines along the long side of the rice field (Fig. 4).
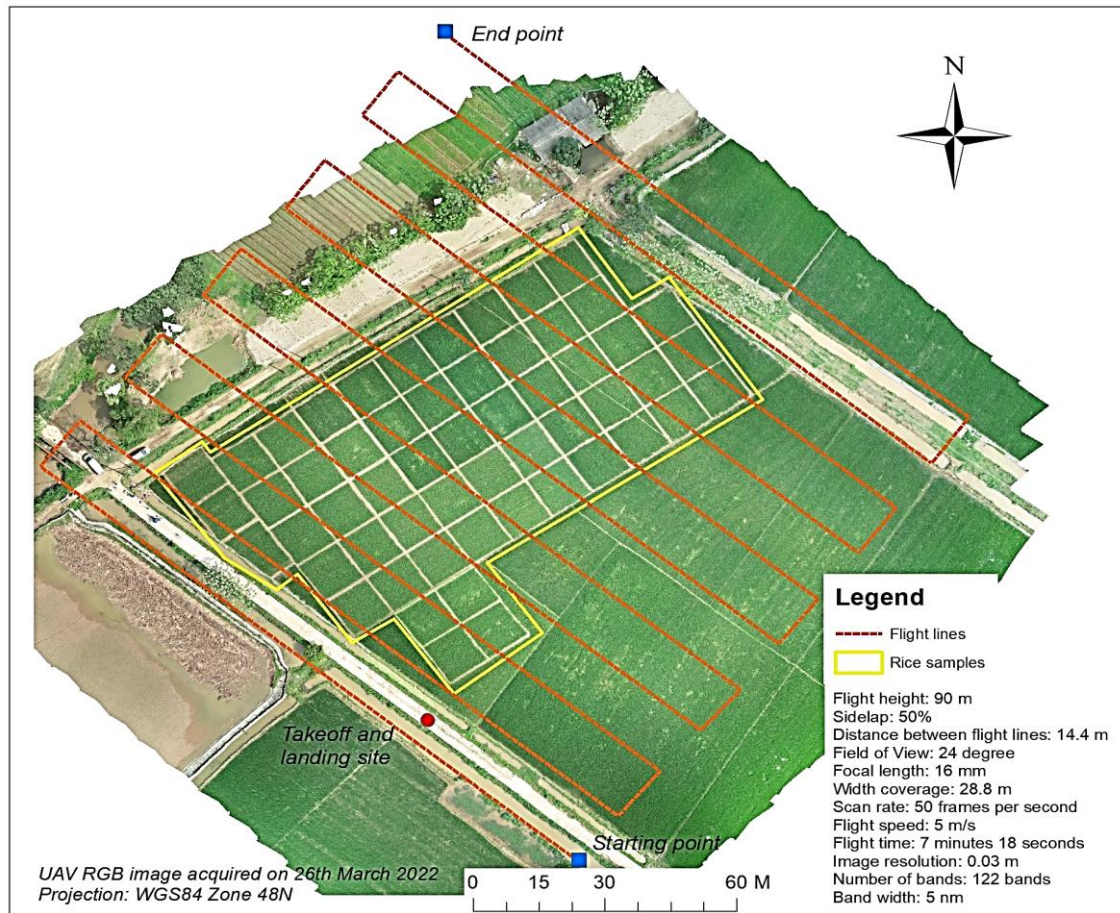

Figure 4. Hyperspectral UAV flight paths and setting parameters for image acquisition

Additionally, the flight duration should be calculated to estimate the appropriate batteries. The flight duration *(E)* is calculated by equation (4).

$$E = \frac{(L * NL + W + D + H' * 4\,)}{V} \qquad (4)$$

where *L* is the length of the long side of the study area; *D* is the distance from the takeoff/landing point (home point) to the start, and the finish points of the flights; *H' * 4* relatively indicates the double distance (takeoff and landing) from ground to the fight height with a plodding speed; *V* is the designed flight speed.

For the study area, the drone flies at 5 m/s. The distances from the home point to the starting point and from the endpoint to the home point are 184 m and 50 m, respectively. The estimated duration of the flight mission is 438 seconds, equivalent to 7 minutes and 18 seconds. The duration is much smaller than the flight capacity empowered by a series of batteries (15 minutes); thus, we need only one battery series for the entire flight.

3.2. Setting up the flight

3.2.1. Mechanical calibration

All the components of subsystems must be appropriately assimilated before starting a fight. The mechanical calibration of each piece of equipment has been done before leaving the factories. The users need to calibrate the balance of the whole system since the gimble is plugged into the drone and the data acquisition system is plugged into the gimble. The hyperspectral acquisition system must be adjusted to ensure a nadir viewing of the camera while mounted to the gimble. The gimble's tilt, roll, and pan axes must be manually adjusted to have initial balances. Finally, the orientation of the gimble must be locked to ensure that the scan direction of the camera is perpendicular to the flight paths.

3.2.2. Camera spectral calibration

The spectral reflectance of the surface is calculated according to equation (5) (Geladi et al., 2004). The spectral calibration of the hyperspectral camera is a step to measure the background and reference intensity just before the flights. The background intensity is the spectral reflectance from a dark object, which simulates the case of without photons interacting with the sensor. To measure the background intensity, the camera's lens is fully covered by a black cap to block all the light from outside while the camera continuously records at least 50 image frames. Besides, the camera records spectral intensity reflected from a particular white reference for white calibration. The camera is set up perpendicular to the white reference with the elevation calculated by equation (6). This study's white reference is 21.0 × 29.7 cm, reflecting 95% of incident radiation. The camera has a 24-degree field of view (FOV). Consequently, the camera's elevation should be lower than 45 cm to ensure the white reference fully covers the ground instantaneous field of view (GIFOV). The camera must adjust values of gain and bias parameters to obtain a maximum intensity of 920 for 10-bit of the hyperspectral sensor while measuring white reference to avoid image saturation.

$$T_\lambda = \frac{S_\lambda - D_\lambda}{R_\lambda - D_\lambda} * 100\% \qquad (5)$$

where T_λ is the surface reflectance in percentage at the wavelength λ; S_λ is the reflectance intensity of the surface; D_λ is the background intensity; R_λ is the white reference intensity.

$$h < \frac{d}{2*\tan(\alpha/2)} \qquad (6)$$

where *h* is the elevation of the sensor counted from the white reference; *d* is the diameter of

the white reference; α is the field of view of the camera.

3.3. Taking hyperspectral data and collecting auxiliary data

Hyperspectral data were taken between 10h20' A.M. and 10h30' A.M. on 26 March 2022. During data acquisition, the weather conditions were characterized by thin cloud cover, a wind speed of approximately 3 m/s from the northeast, an air temperature of 27°C, and 70% relative humidity. The camera scanned along flight lines and captured about 2500 imagery frames a line. The flight paths and parameters for acquiring hyperspectral data are illustrated in Fig. 4.

Simultaneously, a Red-Green-Blue (RGB) orthoimage with very high geometric accuracy (0.04 m of RMSE), 0.01 m spatial resolution, acquired by UAV-RGB camera, was used as a reference image for the hyperspectral geometric correction.

Additionally, spectral reflectance data from three field points within each rice parcel were measured using a handheld ASD Fieldspec 4 spectrometer after immediately acquiring UAV images. A total of 162 spectral reflectance measurements were used for the spectral correction of the hyperspectral images.

Subsequently, rice leaves from the exact locations as the spectral measurements were collected for LPC and LKC chemical analysis. To construct the nutrient estimation model from hyperspectral images, 162 LPC values and 162 LKC values from rice leaves were extracted within 54 rice parcels. Moreover, LKC and LPC from 4 test points were collected at the surrounding rice fields of local farmers for accurate assessment of the models.

3.4. UAV hyperspectral data corrections

3.4.1. Encountered problems

Preprocessing hyperspectral data is the process of raw hyperspectral data to achieve hyperspectral images with a minimized geometric distortion and the lowest spectral errors. Many problems were encountered during the preprocessing steps, including image distortion, light bias, dead pixels, data corruption, spectral noise, and incorrect coordination. The geometric distortion is mainly caused by wind and rotation motions of the UAV during the flights. The gimbal cannot ultimately trace and remove these motions; it can minimize them. The distortion also causes the incorrect coordination of images. Suppose the images are distorted severely (e.g., the positions of image frames are far away from each other). In that case, the program used for processing raw data cannot merge the image frames to create a perfect hyperspectral cube, rendering that cube corrupted. Images acquired from two flight lines are overlaid with a 50% sidelap. The process involves merging the two overlaid images, so-called image stitching. Distinctive features can be found in each image and then efficiently matched to rapidly establish correspondences between pairs of images. However, the light source of the overlaid images is not guaranteed to be identical; stitching two images together can create a visible seam.

For a view consisting of 11 hyperspectral cubes, there are 11 visible seams and 11 areas with different illumination. This effect is later called light bias, a significant issue that must be handled before data analysis. After creating

hyperspectral cubes, some areas appear more significant than the actual size due to distortion, while others appear more minor.

Therefore, unmatched regions appear in the stitched image. Visualization of the problems is shown in Fig. 5.
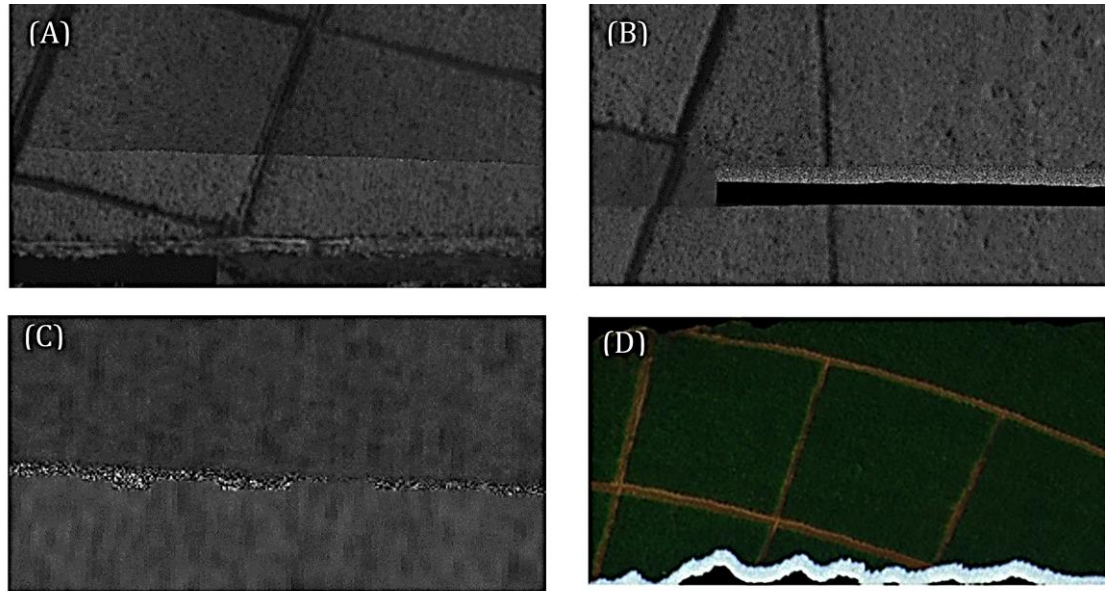

Figure 5. Problems encountered while preprocessing hyperspectral data cubes: (A) Stitched, unmatched, light-biased cubes at the band of 560 nm wavelength; (B) Corrupted cubes cannot be used to merge at the band of 560 nm wavelength; (C) Dead pixels (salt and pepper pixels) between 2 cubes when stitched at the band of 560 nm wavelength; (D) Distorted hyperspectral images of square rice parcels in the nature color composite

3.4.2. Correction method for hyperspectral image

The geometric correction must be done before other processes, such as the spectral correction. The geometric correction uses the reference coordinates extracted from the RGB orthoimage and ground control markers. The coordinates of shape and apparent features appearing in reference and hyperspectral images are also collected for geometric correction. Each hyperspectral spectral cube is individually corrected using a minimum of 10 reference points.

The spectral correction initially uses high-precision handheld spectrometer data measured in selected field points to remove the source bias effect. The measured reflectance power is affected by many factors, which can be described in the following equation (Davies et al., 2022).

$$Simage(\lambda,x,y) = QE(\lambda) \times Toptics(\lambda) \times Tfilter(\lambda) \times Qe(\lambda) \times Robject(\lambda,x,y) \times Geff(\lambda) \quad (7)$$

Where S_{image} is the measured signal of an image pixel. QE is the quantum efficiency of the sensor. T_{optics} is the spectral transmission of the optical system. T_{filter} is the spectral transmission of the filter on the sensor. Q_e is the spectral radiant energy from the light source. R_{object} is the spectral reflectivity of each point in the scene, and G_{eff} is the grating efficiency.

Most of the factors have been factored out during the first calibration using white and

541

black references, but the factor Q_e depends on the instant light source of the system and cannot be factored out. Spectrometer-measured results work as references to calibrate the whole images according to equation 8.

$$S_{calibrated} = S_{image} * \frac{R_{spectrometer}}{S_{fieldpoint}} \quad (8)$$

where $S_{calibrated}$ is the calibrated data of an image, $R_{spectrometer}$ is the averaged reference spectrums of field points, and $S_{fieldpoint}$ is the UAV hyperspectral signals at the corresponding field points. $S_{fieldpoint}$ is taken from hyperspectral cubes as the means of the measured signal of squares of 9 × 9 pixels (or 27 × 27 cm) for every wavelength at field points. The ratios of the references and measurements are the calibration coefficients for the whole image. Consequently, all cubes have balanced reflectance signals if every coefficient is obtained.

3.5. Wavelength selection and vegetation indices

Dealing with the whole spectral domain is very time-consuming and storage-inefficient. Thus, selecting some of the most essential wavelengths for data analysis is necessary. Neighboring bands of a hyperspectral image are usually highly correlated and often provide the same information (Rodarmel and Shan, 2002). The recursive feature elimination

(RFE) method (Pullanagari et al., 2018) is introduced to identify the most critical wavelengths for further analysis. Five models have been chosen consisting of the Least Absolute Shrinkage and Selection Operator (LASSO) regression (Kumar, 2023), Elastic net regression (Giba, 2023), Ridge regression (Granitto et al., 2006; Poona et al., 2016; Kumar, 2023), Random Forest regression (Sruthi, 2024), and Gradient boosting regression (Brownlee, 2020) to perform the RFE method.

Data from 162 field points under the form of a mean value of 81 pixels around each point are passed to the models, and the test is taken to find the most responsive wavelengths with the two parameters P and K. Finally, 10 of the most essential wavelengths is returned by each model for a total of 50 results. Spectral bands with the highest repetition within those 50 results are selected. The most informative wavelengths are used to calculate vegetation indices (Table 1). Vegetation indices that exhibit the strongest correlation with the nutrient concentrations of 162 rice leaf samples are employed to develop the estimation models. These models are then utilized to linearly estimate the Leaf Phosphorus Concentration (LPC) and Leaf Potassium Concentration (LKC) across the rice field.

Table 1. Vegetation indices to monitor plant health

Indexes	Equation
Normalized difference vegetation index (NDVI)	$\frac{R_{NIR} - R_{Red}}{R_{NIR} + R_{Red}}$
Green NDVI (GNDVI)	$\frac{R_{NIR} - R_{Green}}{R_{NIR} + R_{Green}}$
Normalized difference Red-Edge (NDRE)	$\frac{R_{NIR} - R_{Rededge}}{R_{NIR} + R_{Rededge}}$
Modified soil adjusted vegetation index (MSAVI)	$\frac{2R_{NIR} + 1 - \sqrt{(2R_{NIR}+1)^2 - 8(R_{NIR}-R_{Red})}}{2}$
Renormalized difference vegetation index (RDVI)	$\frac{R_{NIR} - R_{Red}}{\sqrt{R_{NIR} + R_{Red}}}$

4. Results

4.1. Corrected UAV hyperspectral images

The hyperspectral image, generated by stitching raw data, comprises 122 spectral bands evenly distributed across a wavelength range of 400 nm to 960 nm. The data is encoded with 10-bit surface spectral reflectance values and lacks geometric coordinate information. Figure 6 illustrates hyperspectral images before doing corrections (A) and after corrections (B). The image before corrections shows different brightness levels between image strips. The divergent brightness levels gradually decrease from the bottom to the top of each image strip (Fig. 6A).
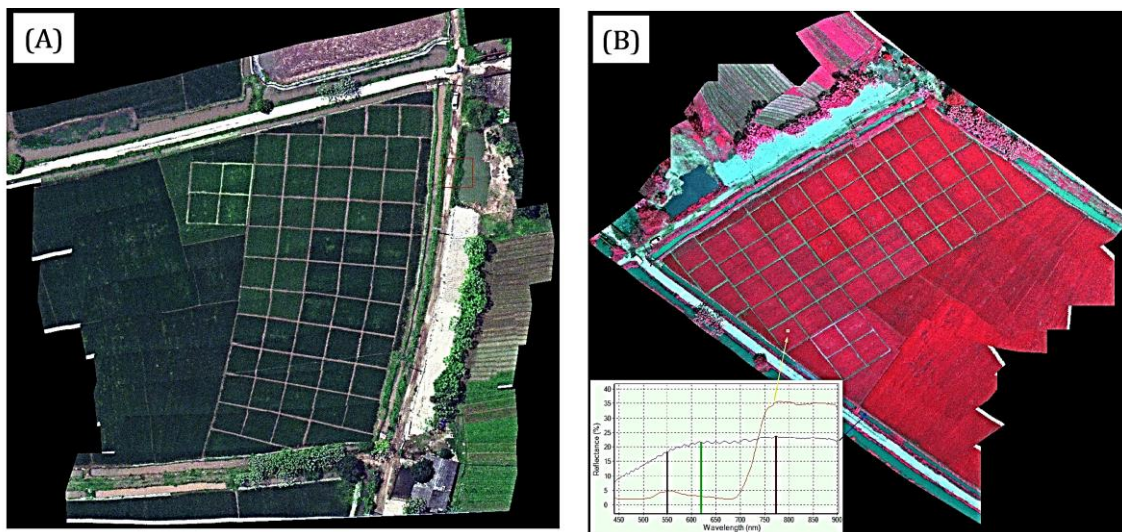

Figure 6. (A) The stitched hyperspectral image of the rice field before corrections. (B) Hyperspectral image in the pseudo color composition of Red, Green, and Blue assigned by bands with wavelengths 770 nm, 620 nm, and 550 nm, respectively, after geometric correction and spectral correction (yellow and blue curves corresponding to spectral reflectance in the range from 437 nm to 900 nm of rice and bare soil in the hyperspectral image)

Additionally, the lines separating rice parcels are not straight, and the areas of parcels are not equal as they are. Under the effect of distortion, the area between the outermost paths to the right of the field was enlarged. Therefore, these paths appear to be more separated as we reach the bottom of the image. The spectral and geometric distortions are the consequence of the unstable camera during the flight and the change of flight path. After corrections (Fig. 6B), the effect of light bias has been minimized, rice edges are parallel, and parcels are squared. The unmatching regions can still be observed in the image due to the lack of ground control points. The features selected as control points were usually field corners; although recognizable using bare eyes, the field corners are sometimes not sharp features. Misalignment only happens in the outer region of the study area, which has fewer control points.

Figure 7 compares field spectrometer measurements and the spectral reflectance of UAV hyperspectral images. Coefficient numbers are ratios between two data sets from

six field points in the parcels T4 and T8. Generally, spectral bands with wavelength range from 400 nm to 437 nm and 900 nm to 960 nm are not used since the coefficient is much greater than 1. Other bands, from 437 nm to 700 nm, show a minor fluctuation, which means that the measurements using the spectrometer agree sufficiently with the UAV results. The remaining part of the spectra, from 700 nm to 900 nm, indicates the fitting between UAV data and spectrometer data with a coefficient of around 1. Figure 6B illustrates the fully corrected image after applying Equation (8) for image bands from band 7 to band 109 corresponding to the wavelengths from 437 nm to 900 nm. Consequently, a hyperspectral image with 103 bands is used for further processes to estimate LKC and LPC of rice.
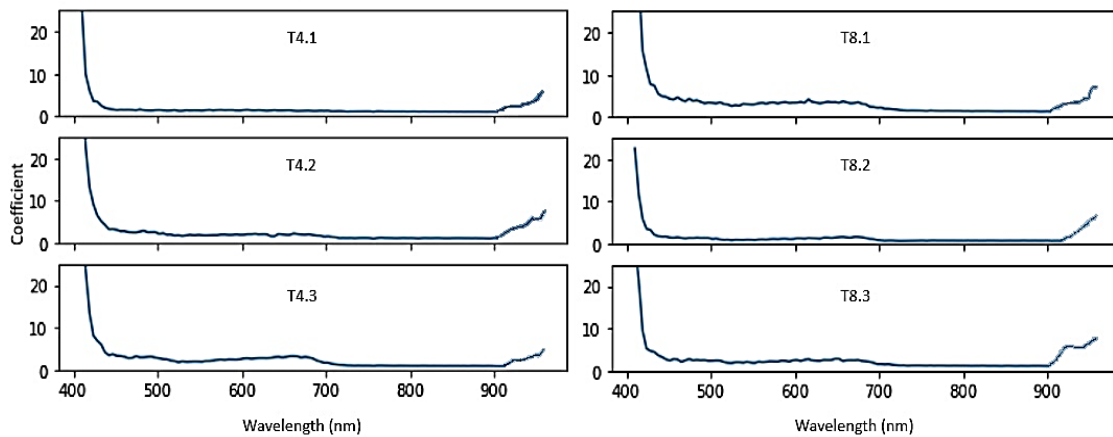

Figure 7. The spectral coefficient calculated by the ratio between field spectrometer measurement and hyperspectral images of 3 points T4.1, T4.2, T4.3 in the T4 parcel and 3 points T8.1, T8.2, T8.3 in the T8 parcel

4.2. Wavelengths and vegetation indices used for estimating LPC and LKC

Table 2 indicates the results of using the recursive features elimination method for hyperspectral data to coordinate the essential features (spectral bands). The five models' most significant spectral bands are in the near-infrared and red domains. Vegetation indices are mainly calculated from four spectral domains: the Green, the Red, the Red-edge, and the Near-infrared. The red edge region is the transition region between red and infrared domains where the spectral reflectance of plants changes rapidly. The green range is evoked mainly by wavelengths from 495 to 570 nm. For each region nominated, we select only two wavelengths with the highest vote by five models in recursive feature elimination to put into computing. Those are 838 nm and 802 nm corresponding to bands 95 and 87 for the NIR wavelength; 734 nm and 721 nm or bands 72 and 69 for the Red-edge wavelength; 635 nm and 607 nm corresponding to bands 44 and 50 for the Red; 566 nm and 539 nm corresponding to band 35 and 29 for the Green. The selected wavelength bands are used to calculate vegetation indices to investigate the nutrient concentration further.

Table 2. Resultant wavelengths from recursive feature elimination

Times selected by models	Wavelengths (nm)				
	Near-Infrared	Red-Edge	Red	Green	Blue
4	838, 802				
3	797, 779		635, 607		
2	856		639, 666	566, 539	442, 456
1	865, 860, 815	734, 721	671, 630, 689, 612	525, 571, 584	488, 475

4.3. LPC and LKC estimated in the rice field

Tables 3 and 4 contain expressions of vegetation indices and correlation coefficients corresponding to phosphorous and potassium concentration in rice leaves. Each of the indices utilizes wavelengths in two regions of the electromagnetic spectrum, and two bands are selected for each region. Subsequently, four results are calculated for every vegetation index, but only indices with the highest correlation are displayed. Generally, the vegetation indices correlate insignificantly with nutrient concentration. The highest correlation to LPC comes from NDRE 838 734 with the correlation coefficient r = 0.401. The correlation coefficient of GNDVI is 0.379. The other indices return an r value with LPC less than 0.3. NDRE, with a correlation of 0.401, is acceptable and can be used to estimate LPC.

Table 3. Vegetation indices correlate the most in their group with phosphorous concentration in rice leaves

Vegetation Index	Expression	Pearson's correlation coefficient (r)
NDVI 838 607	$\dfrac{R_{838nm} - R_{607nm}}{R_{838nm} + R_{607nm}}$	0.292
GNDVI 838 539	$\dfrac{R_{838nm} - R_{539nm}}{R_{838nm} + R_{539nm}}$	0.379
NDRE 838 734	$\dfrac{R_{838nm} - R_{734nm}}{R_{838nm} + R_{734nm}}$	0.401
MSAVI 838 635	$\dfrac{2R_{838nm} + 1 - \sqrt{(2R_{838nm} + 1)^2 - 8(R_{838nm} - R_{635nm})}}{2}$	0.221
RDVI 838 607	$\dfrac{R_{838nm} - R_{607nm}}{\sqrt{R_{838nm} + R_{607nm}}}$	0.241

Table 4. Vegetation indices that correlate the most in their group with potassium concentration in rice leaves

Vegetation index	Expression	Pearson's correlation coefficient (r)
NDVI 802 607	$\dfrac{R_{802nm} - R_{607nm}}{R_{802nm} + R_{607nm}}$	-0.328
GNDVI 838 566	$\dfrac{R_{838nm} - R_{566nm}}{R_{838nm} + R_{566nm}}$	-0.325
NDRE 802 721	$\dfrac{R_{802nm} - R_{721nm}}{R_{802nm} + R_{721nm}}$	-0.323
MSAVI 802 635	$\dfrac{2R_{802nm} + 1 - \sqrt{(2R_{802nm} + 1)^2 - 8(R_{802nm} - R_{635nm})}}{2}$	-0.237
RDVI 802 635	$\dfrac{R_{802nm} - R_{635nm}}{\sqrt{R_{802nm} + R_{635nm}}}$	-0.261

The NDVI 802 607 is the most correlated vegetation index with a r = -0.328 for LKC. LKC correlates negatively with every index proposed. MSAVI correlates the least with LKC, with r ranging from -0.233 to -0.237. RDVI follows MSAVI, with r lying between -0.254 to -0.261. NDRE, GNDVI, and NDVI all show the same level of relationship with LKC, with the r value varying from -0.3 to -0.328. The most corresponding indexes to LPC and LKC with their linear equations are represented in Fig. 8.
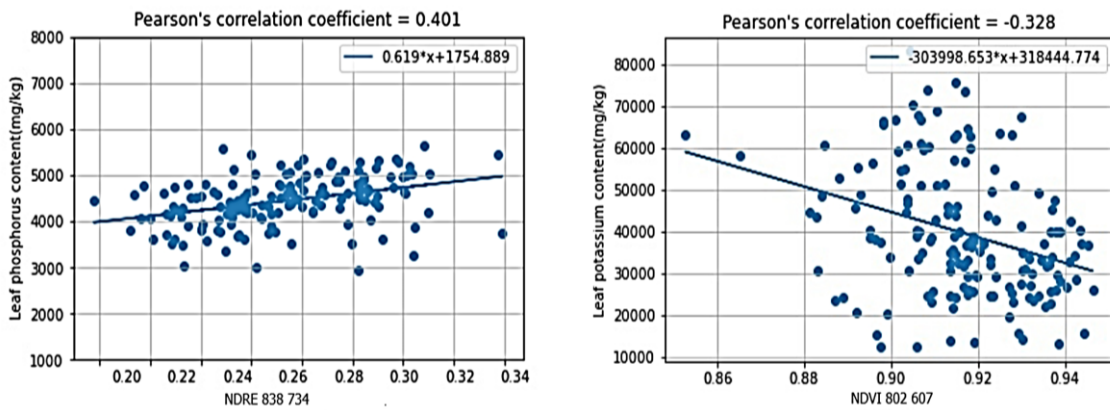

Figure 8. The relationship between (A) NDRE composed of 838 nm and 734 nm wavelength bands and LPC, (B) NDVI composed of 802 nm and 607 nm wavelength bands and LKC

Figure 9A and Fig. 9B illustrate LKC and LPC concentration in rice leaves using the linear regressions obtained from the indexes NDVI 802 607 and NDRE 838 734, respectively. The maps show blatant discrimination between LKC and LPC. A higher LKC is seen in the J02 rice species (J letter in Fig. 1). However, it's a reversed case in LPC, as the higher LPK belongs to TBR225 parcels. The quantitative difference between LKC and LPC is indicated in Fig. 10. Figure 10 shows the box diagrams of nutrient concentration for two rice varieties. The undermost lines, the box's undermost lines, and the yellow lines represent the minimum given value, the median of the lower half, and the median of the dataset, respectively. The two uppermost lines illustrate the counterparts of the two undermost lines. Generally, LKC for TBR225 is typically higher than that of J02, while the opposite happens for LPC. This study used LKC and LPC of four test points in the farmer's field surrounding rice sample plots to assess the accuracy of estimation models. The model for LPC returns a root mean squared error (RMSE) of 27.1%, while the estimating model for LKC has an RMSE of 38.8%.
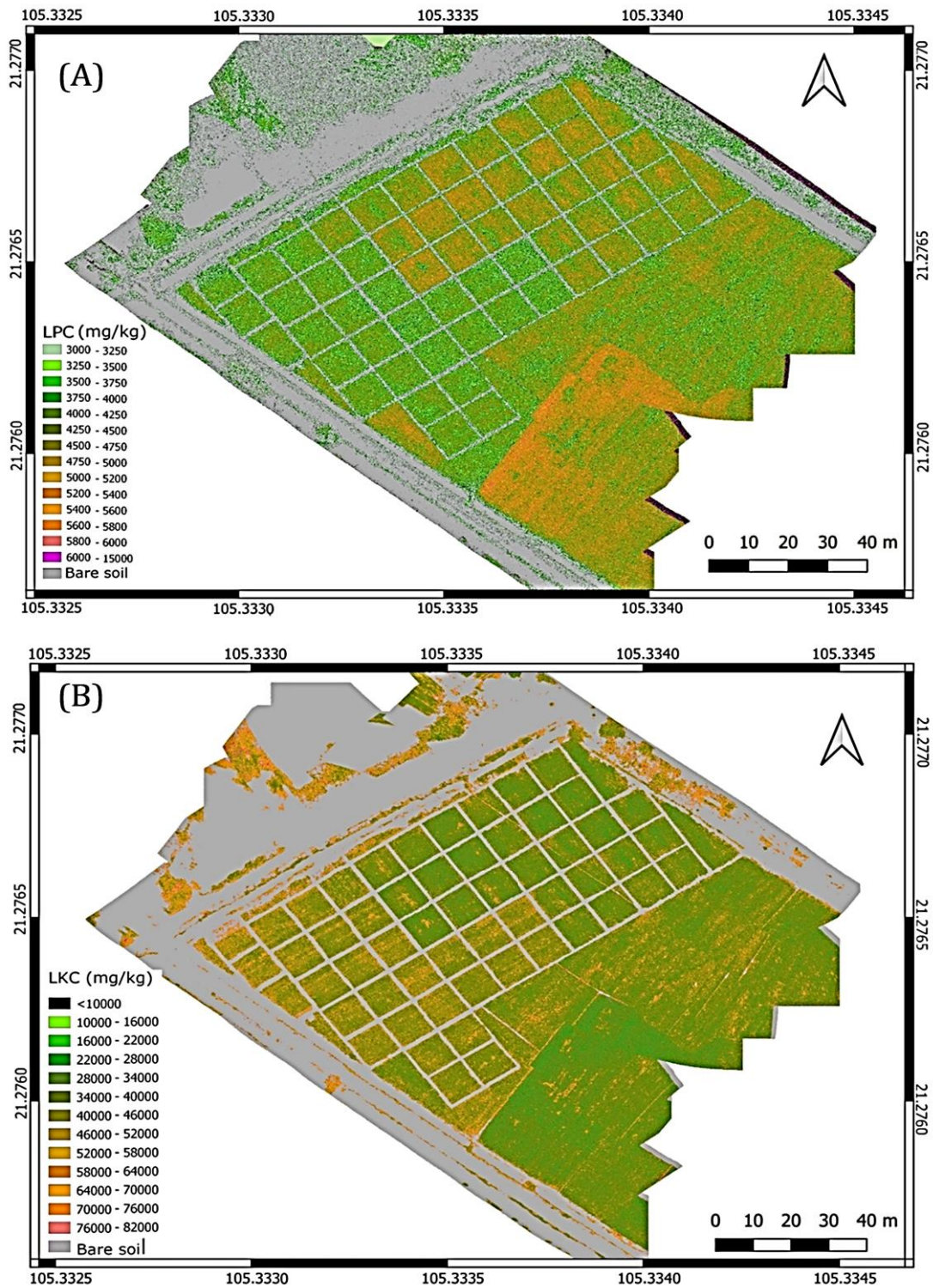
Figure 9. Map of (A) estimation of LPC using NDRE 838-734 index, and (B) estimation of LKC using NDVI 802-607
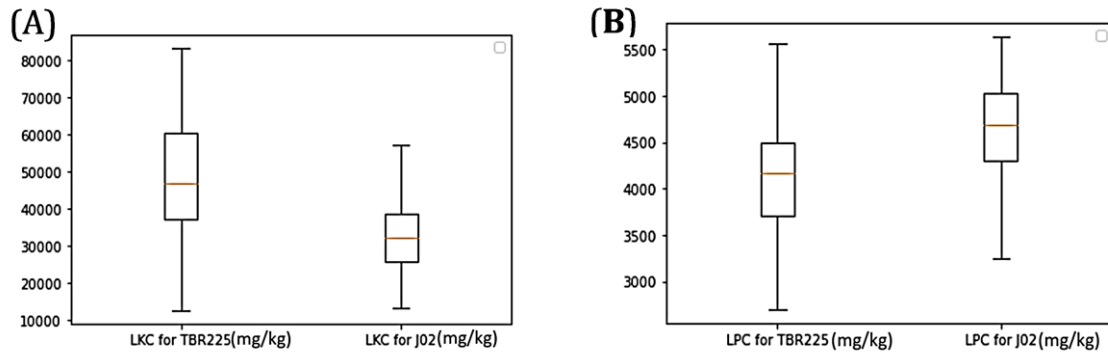
Figure 10. Nutrient distributions of rice varieties, displayed in box plots with outliers removed, (A) Distribution of LKC for two rice variants, (B) Distribution of LPC for two rice variants

5. Discussions

Hyperspectral data acquisition via UAVs presents distinct advantages, including flexible acquisition timing, reduced atmospheric interference compared to satellite-based platforms, and achieving hyperspectral images with very high spatial resolution (centimeter level). Nevertheless, the utilization of UAVs for hyperspectral data acquisition is confronted with several challenges associated with the mechanical integration of the UAV-Gimbal-Sensor system, geometric correction processes, and the spectral calibration of hyperspectral data. The absence of an automated system for synchronizing the movements of UAVs, gimbals, and sensors during hyperspectral data scanning presents a significant challenge in the pre-flight installation process. Typically, the gimbal must be manually configured to ensure that the scanning direction of the sensor remains parallel to the flight lines in the designated field (Fig. 4). To facilitate this alignment, flight lines are ideally designed parallel to linear features such as straight roads, simplifying the definition of scanning direction in the field. When a straight road is unavailable, a makeshift linear object, such as a toilet roll, can temporarily guide the camera and gimbal for accurate alignment.

Geometrical distortion may manifest in the hyperspectral cube (ex. Fig. 5), attributed to imperfectly aligned coordinates from GNSS receivers to the data frames (Skiles et al., 2023). In addressing this issue, using UAV photogrammetry to generate RGB orthoimages as a reference image for the georectification of hyperspectral cubes is preferred over using a series of ground control point (GCP) markers. The RGB orthoimage, acquired concurrently with hyperspectral data using UAV-RTK technology, exhibits millimeter-level resolution, achieves exceptionally high geographical accuracy, and potentially provides reference coordinates due to the ease of identifying identical objects. Therefore, using an RGB orthoimage for geo-correcting hyperspectral images minimizes effort compared to utilizing GCP markers.

The primary challenge in generating hyperspectral cubes from UAV-based data lies in mitigating atmospheric effects despite the UAVs operating beneath the cloud layer. The brief 2-minute flight duration for each flight line introduces variability in atmospheric conditions due to dynamic factors such as clouds, fog, or wind leading to fluctuations in incident radiation on the land surface. Relying solely on the unique white calibration of the camera performed before UAV takeoff proves inadequate for fully processing all spectral cubes. While using ground spectrometer measurements may be sufficient in the current study, integrating a spectrometer into the UAV

548

for real-time spectral calibration of the hyperspectral camera emerges as a potential solution for future endeavors. Despite some residual bias in the results, UAV-based hyperspectral data remains the predominant methodology to fill the existing gap in satellite-based hyperspectral data.

The index NDRE 838 734 indicates a maximum correlation of r = 0.401 with LPC, consistent with previous studies (Mahajan et al. 2016, Pinit et al. 2022, Zhang et al. 2023). The positive correlation between red-edge wavelengths (670-760 nm) and LPC is explained by the concentration of anthocyanins in leaves. Anthocyanins, being water-soluble pigments, reflect the spectral wavelength at around 550 nm and 800 nm but not at 700 nm (Gitelson et al. 2009, Zhang et al. 2023). The concurrence of reflectance peaks at 550 nm and 800 nm are the same wavelengths with chlorophyll reflectance properties. In this study, the subtraction of the 734 nm wavelength in the NDRE 838 734 index isolates the contribution of anthocyanins. Notably, the variability in phosphorus levels is identified as a stimulant for anthocyanin concentration (Jiang et al., 2007; Li et al., 2023). Consequently, NDRE 838 734 is an appropriate approach for estimating LPC in rice leaves.

In contrast to the behavior exhibited by LPC and spectral reflectance, LKC demonstrates a negative correlation with vegetation indices. Despite attempts to predict LKC based on visible (607 nm) and near-infrared wavelength (802 nm), the effectiveness is compromised by a weak correlation, reaching a maximum of r = -0.328. This outcome aligns with the findings reported by Albayrak (2008) and Lu et al. (2020), suggesting that the challenging investigation of LKC in vegetation arises from the overlapping regions of nitrogen- and potassium-sensitive wavelengths (Albayrak, 2008; Lu et al., 2019). The integration of visible and near-infrared bands in vegetation indices proves to be more responsive to nitrogen content or plant pigments than to potassium content (Liu et al., 2019; Wang et al., 2021). Furthermore, the water content in leaves positively correlates with potassium ions around the guard cells (Nieves-Cordones et al., 2014). As relative water concentration increases, the absorption in near-infrared and short-wave infrared regions increases, reducing the reflectance at these wavelength regions. However, the negative relationship between water concentration and the reduction of the short-wave infrared reflectance is much more significant than near-infrared (Das et al., 2017). Thus, the promising wavelengths for rice LKC monitoring are supposed to be short-wave infrared regions (Lu et al., 2019).

The assessment of LPC and LKC by applying UAV hyperspectral data in this investigation yields notable discrepancies (RMS error of 27.1% for LPC and 38.8% for LKC). Besides the technical challenges associated with the acquired data, accuracy is inherently influenced by the complex interplay of various factors governing characteristic reflectance. These factors encompass chlorophyll and other light-absorbing pigments, water content, proteins, starches, waxes, and structural and biochemical molecules like lignin and cellulose, which are ubiquitous in vegetation (Lu et al. 2020). Consequently, the specific estimation of nutrient concentrations such as phosphorus or potassium in leaves proves challenging. Integrating hyperspectral data with deep learning algorithms as convolutional neural networks (Nalepa et al., 2020) or DeepSpectra (Zhang et al., 2019) is a promising solution for enhancing accuracy. Collecting extensive datasets to employ deep learning models effectively is implemented to estimate leave nutrient concentrations in future studies. Subsequently, the development of software incorporating deep learning

549

techniques is ideally anticipated, which will facilitate the map of nutrient levels in hyperspectral images collected from broad rice fields.

6. Conclusions

This study provides instructions for using UAVs integrated hyperspectral cameras for nutrient content monitoring in rice leaves, one of Vietnam's most essential food types of crops. The experiment demonstrated the ability to use UAV-based remote sensing to quantify rice plants' phosphorous and potassium deficiencies in a label-free, noninvasive, and non-destructive manner. Although the relationship between phosphorus content in rice leaves and rice spectral footprint between 400 nm and 1000 nm is not very strong, a relationship between the NDRE index and LPC has been found with a correlation of r=0.401. A linear regression model for estimating LPC from the NDRE index has been built with an estimative capability of 27.1% RMSE. LKC can be estimated from the NDVI index using wavelengths of 802 nm and 607 nm with an acceptable accuracy.

From the experiment, several recommendations for future studies are identified. Firstly, a hyperspectral camera with an expanded spectral range, specifically between 900 and 2500 nm, is suggested for investigating LKC, and other chemical components. Secondly, integrating measurement data and hyperspectral data into deep learning models is proposed as a promising method to enhance the accuracy of nutrient estimation. Many field measurements in various rice crops should be collected for the deep learning approach. Thirdly, deploying a UAV system for data acquisition and processing is complex. Tasks such as calculating flight parameters, designing flight paths, and calibrating images are manually performed by researchers, while the software integrated into drones handles the actual flight according to these parameters. This study offers a comprehensive overview of the integration of components within a UAV hyperspectral system. The methodologies outlined in this study can be effectively utilized for various applications within earth sciences and environmental monitoring domains. Furthermore, this research is pioneering the use of UAV hyperspectral technology to assess vegetation health in Vietnam, an agriculturally significant nation.

Acknowledgments

References

Adão T., J. Hruška, L. Pádua, J. Bessa, E. Peres, R. Morais, J. Sousa. 2017. Hyperspectral Imaging: A Review on UAV-Based Sensors, Data Processing and Applications for Agriculture and Forestry. Remote Sensing, 9(11), 1110.

Albayrak S., 2008. Use of Reflectance Measurements for the Detection of N, P, K, ADF and NDF Contents in Sainfoin Pasture. Sensors (Basel), 8(11), 7275–7286.

Brownlee J., 2020. Feature Importance and Feature Selection With XGBoost in Python. from https://machinelearningmastery.com/feature-importance-and-feature-selection-with-xgboost-in-python/.

Buresh R., 2022. Rice Knowledge Bank, Nitrogen (N) excess. from http://www.knowledgebank.irri.org/training/fact-sheets/nutrient-management/deficiencies-and-toxicities-fact-sheet/item/nitrogen-excess#:~:text=What%20it%20does,the%20strength%20of%20the%20stems.%20.

Campos-Soriano L., M. Bundo, M. Bach-Pages, S.F. Chiang, T.J. Chiou, B. San Segundo, 2020. Phosphate excess increases susceptibility to

pathogen infection in rice. Mol Plant Pathol, 21(4), 555–570.

Chang, Chein- I., 2003. Hyperspectral Imaging: Techniques for Spectral Detection and Classification. New York: Kluwer Academic/Plenum Publishers.

Clauss K., M. Ottinger, P. Leinenkugel, C. Kuenzer, 2018. Estimating rice production in the Mekong Delta, Vietnam, utilizing time series of Sentinel-1 SAR data. International Journal of Applied Earth Observation and Geoinformation, 73, 574–585.

Das B., R.N. Sahoo, S. Pargal, G. Krishna, R. Verma, V. Chinnusamy, V.K. Sehgal, V.K. Gupta, 2017. Comparison of different uni- and multi-variate techniques for monitoring leaf water status as an indicator of water-deficit stress in wheat through spectroscopy. Biosystems Engineering, 160, 69–83.

Davies M., M.B. Stuart, M.J. Hobbs, A.J.S. McGonigle, J.R. Willmott, 2022. Image Correction and In Situ Spectral Calibration for Low-Cost, Smartphone Hyperspectral Imaging. Remote Sensing, 14(5), 1152.

Delavarpour N., C. Koparan, J. Nowatzki, S. Bajwa, X. Sun, 2021. A Technical Study on UAV Characteristics for Precision Agriculture Applications and Associated Practical Challenges. Remote Sensing, 13(6), 1204.

Dobermann A., T. Fairhurst, 2000. Rice: Nutrient Disorders & Nutrient Management, Potash & Phosphate Institute, East & Southeast Asia Programs. ISBN 981-04-2742-5.

Geladi P., J. Burger, T. Lestander, 2004. Hyperspectral imaging: calibration problems and solutions. Chemometrics and Intelligent Laboratory Systems, 72(2), 209–217.

Giba L., 2023. Elastic Net Regression Explained, Step by Step. from https://machinelearningcompass.com/machine_learning_models/elastic_net_regression/.

Gitelson A.A., O.B. Chivkunova, M.N. Merzlyak, 2009. Nondestructive estimation of anthocyanins and chlorophylls in anthocyanic leaves. Am. J. Bot., 96(10), 1861–1868.

Grahn H., P. Geladi, 2007. Techniques and Applications of Hyperspectral Image Analysis. Wiley & Sons, Ltd. https://doi.org/10.1002/9780470010884.

Granitto P.M., C. Furlanello, F. Biasioli, F. Gasperi, 2006. Recursive feature elimination with random forest for PTR-MS analysis of agroindustrial products. Chemometrics and Intelligent Laboratory Systems, 83(2), 83–90.

Hindersah R., A.M. Kalay, A. Talahaturuson, 2022. Rice yield grown in different fertilizer combination and planting methods: Case study in Buru Island, Indonesia. Open Agriculture, 7(1), 871–881.

Jiang C., X. Gao, L. Liao, N.P. Harberd, X. Fu, 2007. Phosphate starvation root architecture and anthocyanin accumulation responses are modulated by the gibberellin-DELLA signaling pathway in Arabidopsis. Plant Physiol, 145(4), 1460–1470.

Kumar D., 2024. A Complete understanding of LASSO Regression. from https://www.mygreatlearning.com/blog/understanding-of-lasso-regression/

Li H., K. He, Z. Zhang, Y. Hu, 2023. Molecular mechanism of phosphorous signaling inducing anthocyanin accumulation in Arabidopsis. Plant Physiology and Biochemistry, 196, 121–129.

Ling B., D.G. Goodin, E.J. Raynor, A. Joern, 2019. Hyperspectral Analysis of Leaf Pigments and Nutritional Elements in Tallgrass Prairie Vegetation. Frontiers in Plant Science, 10, 142. https://doi.org/10.3389/fpls.2019.00142.

Liu H., H. Zhu, Z. Li, G. Yang, 2019. Quantitative analysis and hyperspectral remote sensing of the nitrogen nutrition index in winter wheat. International Journal of Remote Sensing, 41(3), 858–881.

Lu J., W. Li, M. Yu, X. Zhang, Y. Ma, X. Su, X. Yao, T. Cheng, Y. Zhu, W. Cao, Y. Tian, 2020. Estimation of rice plant potassium accumulation based on non-negative matrix factorization using hyperspectral reflectance. Precision Agriculture, 22(1), 51–74.

Lu J., T. Yang, X. Su, H. Qi, X. Yao, T. Cheng, Y. Zhu, W. Cao, Y. Tian, 2019. Monitoring leaf potassium content using hyperspectral vegetation indices in rice leaves. Precision Agriculture, 21(2), 324–348.

Mahajan G.R., R.N. Pandey, R.N. Sahoo, V.K. Gupta, S.C. Datta, D. Kumar, 2016. Monitoring nitrogen, phosphorus and sulphur in hybrid rice (Oryza sativa

L.) using hyperspectral remote sensing. Precision Agriculture, 18(5), 736–761.

Nalepa J., M. Antoniak, M. Myller, P. Ribalta Lorenzo, M. Marcinkiewicz, 2020. Towards resource-frugal deep convolutional neural networks for hyperspectral image segmentation. Microprocessors and Microsystems, 73, 102994.

Nguyen D., K. Clauss, S. Cao, V. Naeimi, C. Kuenzer, W. Wagner, 2015. Mapping Rice Seasonality in the Mekong Delta with Multi-Year Envisat ASAR WSM Data. Remote Sensing, 7(12), 15868–15893.

Nieves-Cordones M., F. Aleman, V. Martinez, F. Rubio, 2014. K^+ uptake in plant roots. The systems involved, their regulation and parallels in other organisms. J. Plant Physiol, 171(9), 688–695.

Phung H.-P., L.-D. Nguyen, N.-H. Thong, L.-T. Thuy, A.A. Apan, 2020. Monitoring rice growth status in the Mekong Delta, Vietnam using multitemporal Sentinel-1 data. Journal of Applied Remote Sensing, 14(01), 1.

Pinit S., N. Ruengchaijatuporn, S. Sriswasdi, T. Buaboocha, S. Chadchawan, J. Chaiwanon, 2022. Hyperspectral and genome-wide association analyses of leaf phosphorus status in local Thai indica rice. PLoS One, 17(4), e0267304.

Poona N.K., A. van Niekerk, R.L. Nadel, R. Ismail, 2016. Random Forest (RF) Wrappers for Waveband Selection and Classification of Hyperspectral Data. Applied Spectroscopy, 70(2), 322–333.

Pullanagari R., G. Kereszturi, I. Yule, 2018. Integrating Airborne Hyperspectral, Topographic, and Soil Data for Estimating Pasture Quality Using Recursive Feature Elimination with Random Forest Regression. Remote Sensing, 10(7), 1117.

Rodarmel C., J. Shan, 2002. Principal Component Analysis for Hyperspectral Image Classification. Surveying and Land Information Science, 62(2), 115–123.

Sanchez L., A. Ermolenkov, S. Biswas, E.M. Septiningsih, D. Kurouski, 2020. Raman Spectroscopy Enables Noninvasive and Confirmatory Diagnostics of Salinity Stresses, Nitrogen, Phosphorus, and Potassium Deficiencies in Rice. Front Plant Sci., 11, 573321.

Skiles S.M., C.P. Donahue, A.G. Hunsaker, J.M. Jacobs, 2023. UAV hyperspectral imaging for multiscale assessment of Landsat 9 snow grain size and albedo. Frontiers in Remote Sensing, 3:1038287. doi: 10.3389/frsen.2022.1038287.

Sruthi E.R., 2024. Understand Random Forest Algorithms With Examples (Updated 2024). Analytics Vidhya. From https://www.analyticsvidhya.com/blog/2021/06/understanding-random-forest/

Stuart B.H., 2021. Infrared Spectroscopy of Biological Applications: An Overview. Encyclopedia of Analytical Chemistry, 1–16.

Wallach O., 2022. Visualizing the World's Biggest Rice Producers. from https://www.visualcapitalist.com/worlds-biggest-rice-producers/#google_vignette.

Wang L., S. Chen, D. Li, C. Wang, H. Jiang, Q. Zheng, Z. Peng, 2021. Estimation of Paddy Rice Nitrogen Content and Accumulation Both at Leaf and Plant Levels from UAV Hyperspectral Imagery. Remote Sensing, 13(15), 2956.

Zhang X., T. Lin, J. Xu, X. Luo, Y. Ying, 2019. DeepSpectra: An end-to-end deep learning approach for quantitative spectral analysis. Analytica Chimica Acta, 1058, 48–57.

Zhang Y., T. Wang, Z. Li, T. Wang, N. Cao, 2023. Based on machine learning algorithms for estimating leaf phosphorus concentration of rice using optimized spectral indices and continuous wavelet transform." Front Plant Sci., 14, 1185915.

Zhang Z., D. Jiang, Q. Chang, Z. Zheng, X. Fu, K. Li, H. Mo, 2023. Estimation of Anthocyanins in Leaves of Trees with Apple Mosaic Disease Based on Hyperspectral Data. Remote Sensing, 15(7), 1732.